

18 Abstract

19 Image-based pore-scale modeling is an important method to study multiphase flow in permeable
20 rocks. However, in many rocks, the pore size distribution is so wide that it cannot be resolved in a
21 single pore-space image, typically acquired using micro-computed tomography (micro-CT).
22 Recent multi-scale models therefore incorporate sub-voxel porosity maps, created by differential
23 micro-CT imaging of a contrast fluid in the pores. These maps delineate different microporous
24 flow zones in the model, which must be assigned petrophysical properties as input. The uncertainty
25 on the pore scale physics in these models is therefore heightened by uncertainties on the
26 representation of unresolved pores, also called sub-rock typing. Here, we address this by validating
27 a multi-scale pore network model using a drainage experiment imaged with differential micro-CT
28 on an Estailades limestone sample. We find that porosity map-based sub-rock typing was unable
29 to match the micrometer-scale experimental fluid distributions. To investigate why, we introduce
30 a novel baseline sub-rock typing method, based on a 3D map of the experimental capillary pressure
31 function. By incorporating this data, we successfully remove most of the sub-rock typing
32 uncertainty from the model, obtaining a close fit to the experimental fluid distributions.
33 Comparison between the two methods shows that in this sample, the porosity map is poorly
34 correlated to the multiphase flow behavior of the microporosity. The validation method introduced
35 in this paper serves to separate and address the uncertainties in multi-scale models, facilitating
36 simulations in complex geological reservoir rocks important for e.g. geological storage of CO₂ and
37 renewable energy.

38

39 Plain Language Summary

40 Understanding multiphase flow within heterogeneous reservoir rocks is crucial for geological
41 reservoir management. These rocks usually have intricate microstructures (unresolved or sub-
42 resolution pores) which are difficult to quantify and have a strong impact on fluid flow. Pore-scale
43 modelling combined with imaged-based experiments can be a useful tool to describe complex pore
44 structures, which is of key importance in the subsequent simulation and prediction of multiphase
45 flow behavior. In this study, we focus on improving the representation of unresolved porous
46 regions of a heterogeneous rock sample (also called sub-rock typing). A drainage experiment was
47 performed and imaged by micro-computed tomography (micro-CT) to characterize the multiphase

48 distribution at increasing capillary pressures. The predictions of two multi-scale models, which
49 were generated according to distinct sub-rock typing methods on the same sample, were compared
50 with the drainage experimental data. We found that the model obtained by the “classical” sub-rock
51 typing method was unable to simulate the correct arrangement of fluids in this sample, while the
52 new method performed better, which illustrates the importance of rock type identification to pore-
53 scale modelling. The validation workflow presented in this paper can be extended and served as a
54 reliable reference to improve simulations in other complex geological materials.

55 **1 Introduction**

56 Multiphase flow through rocks plays an important role in numerous earth science applications,
57 such as hydrocarbon recovery (Olayiwola & Dejam, 2019; Wang et al., 2020), carbon dioxide
58 storage (Arif et al., 2017), remediation of polluted aquifers (Bortone et al., 2013) and subsurface
59 energy storage in the form of hydrogen or compressed air (Amid et al., 2016, Mouli-Castillo et al.,
60 2019). Many reservoir rocks, notably carbonates and clay-bearing sandstones, exhibit complex
61 pore geometries with very wide pore size distributions. The petrophysical properties of such rocks
62 often do not obey classical correlations (Prodanović et al., 2015; Shanley et al., 2004), spurring
63 pore-scale studies of their fluid flow behavior (Mehmani et al., 2020). This can be done based on
64 images of the pore space, obtained with for example micro-computed tomography (micro-CT) and
65 (FIB-)SEM imaging (Bultreys et al., 2016b; Bera et al., 2011; Ciobanu et al., 2011; Cnudde &
66 Boone, 2013; Wirth, 2009).

67 Despite the wide interest in simulating fluid flow in complex, multi-scale pore spaces, the trade-
68 off between image size and resolution in most imaging techniques complicates the development
69 of suitable image-based approaches (Blunt et al., 2013). Typical imaging workflows identify
70 resolved pores and zones with unresolved porosity (below the μm scale) in micro-CT images of
71 mm-scale samples, which usually capture the largest pore features. Unresolved porosity is visible
72 in these images as zones with grey values that are intermediate between solid and void, due to their
73 intermediate density (Cnudde & Boone, 2013). These regions can then be imaged by higher-
74 resolution techniques, that are then correlated back to the lower-resolution micro-CT scan (De
75 Boever et al., 2015; Devarapalli et al., 2017; Lin et al., 2019). The unresolved pores, which we
76 will by definition refer to as the microporosity, can play a crucial role in the sample's multiphase
77 flow behavior (Bultreys et al., 2016c; Mehmani et al., 2020). Therefore, specialized multi-scale
78 models are required that fuse the resolved pores with information on the microporosity features,
79 typically obtained using higher-resolution images on small sub-sections of the sample (Menke et
80 al., 2019).

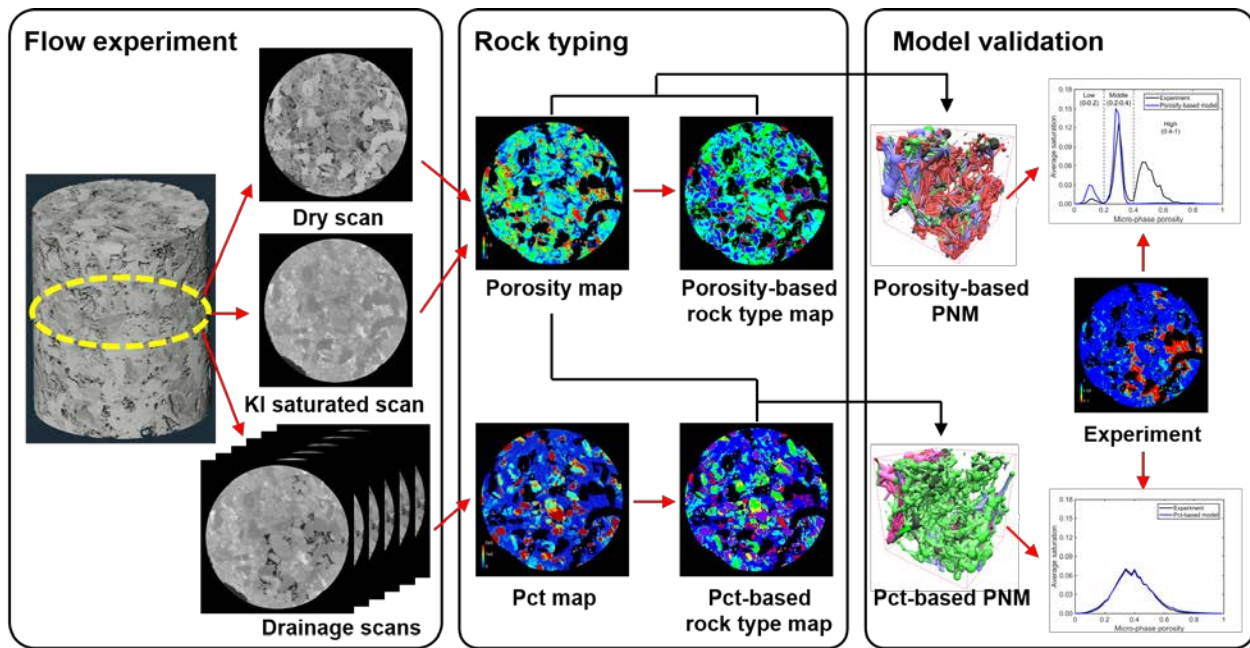
81 Multi-scale models are an extension of pore-scale, image-based modelling techniques, consisting
82 of either direct numerical simulations (Alhashmi et al., 2015; Pan et al., 2004; Raeini et al., 2012)
83 or pore network models (PNMs) (Blunt et al., 2013; Dong & Blunt, 2009). Direct numerical
84 simulations of multiphase flow usually require large computational resources and therefore

85 struggle to capture capillary-dominated flow on large images (Blunt et al., 2013). PNMs feature
86 higher computational efficiencies due to simplifications on the geometry and the fluid
87 displacement physics, which makes them well-suited for multi-scale simulations. Networks
88 obtained at different resolutions or scales can be extrapolated in space and fused to reconstruct a
89 multi-scale pore network (Jiang et al., 2013; Mehmani & Prodanovic, 2014), resulting in detailed
90 but very large networks. Alternatively, the micropores can be treated as a continuous porous
91 medium with specific petrophysical properties to reduce the size of the network while still
92 representing the connectivity caused by microporosity (Bultreys et al., 2015; Bauer et al., 2012;
93 Youssef et al., 2008).

94 Despite the progress in representing multi-scale pore networks, it remains difficult to assess the
95 model uncertainties. Multi-scale pore network models depend on a significant amount of uncertain
96 input information to describe the microporosity behavior, which complicates the validation of the
97 physical assumptions in the model itself (e.g. quasi-static fluid displacement). An important aspect
98 of the input uncertainty is that only a limited volume of microporosity is typically imaged at the
99 highest resolutions, while there is often significant heterogeneity in its properties. Recent
100 approaches have addressed this information gap by incorporating sub-voxel porosity maps
101 (Ruspini et al., 2016, 2021). The porosity map can be generated based on differential imaging:
102 measuring the calibrated grey value change when the pore space is filled with a high-contrast fluid
103 such as high-concentration potassium iodide or cesium chloride (Boone et al., 2014; Ghous et al.,
104 2007, Lin et al., 2016). The resulting map is then used for “sub-rock typing”: identifying and
105 characterizing zones with different microporosity properties in the model. The common approach
106 is to perform a segmentation on dry images or differential images directly to separate distinct
107 phases, sometimes followed by a series of image processing operations to alleviate artifacts at
108 phase boundaries (Bauer et al., 2012; Bultreys et al., 2015). However, there is still a lack of
109 validation to reveal whether these approaches can provide a reasonable representation for
110 unresolved pores and how much uncertainty they introduce into the multi-scale PNM simulations.
111 Recent work on single-scale pore network models has illustrated how pore-by-pore validation of
112 the fluid distributions during drainage or imbibition can serve to study model uncertainties
113 (Bultreys et al., 2018, 2020, Øren et al., 2019). A similar principle used to generate porosity maps
114 can be used to track the fluid saturation in microporous regions during multiphase flow
115 experiments (Lin et al., 2016, Gao et al., 2017). In this paper, we propose a pore-by-pore validation

116 workflow for multi-scale PNM by comparing fluid distributions in the model to a differential
 117 micro-computed tomography (micro-CT) based drainage experiment on a heterogeneous
 118 Estailledes limestone (as shown in Figure 1). Using this data, we validate the porosity-map based
 119 workflow, and explain its uncertainties by comparing to a novel data-based model, which takes its
 120 microporosity information from the micro-CT drainage experiment. The experiment and the image
 121 processing workflows are introduced in Section 2.1. Then, the multiscale PNM workflow
 122 including the two sub-rock typing methodologies (porosity-based and drainage-based methods)
 123 are explained in Section 2.2. In Section 3, we compare the predictions from the two models with
 124 experimental data and discuss the reasons that may lead to simulation uncertainties. Section 4
 125 discusses the conclusion and the outlook for our future research.

126



127

128

129

Figure 1. The validation workflow for multi-scale pore network model.

130 2 Materials and Methods

131 2.1 Experiment

132 The main goal of the experiment presented here is to measure the brine and decane distribution
 133 within both macropores and microporous regions of the sample during capillary drainage. In the

134 following, the sample and fluid preparation, the set-up, the experimental procedure and data
135 processing workflow will be discussed in detail.

136 2.1.1. Rock samples and fluid preparation

137 The rock sample used in the experiment is Estailades limestone, which has a complex pore
138 structure featuring a bi-modal pore size distribution. The broad pore size distribution has two peaks
139 with modes of respectively 390 nm and 19 μm (Han et al., 2007). Estailades limestone is
140 composed of 99% calcite (Alyafei & Blunt, 2016). A sample with a diameter of 6 mm and a length
141 of 20 mm was cored and vacuum-saturated with deionized water to ensure that all the air was
142 removed from the pores before the experiment.

143 As fluid phases in the drainage experiment, we used KI-brine and decane. The former acted as
144 wetting phase, while the latter was the non-wetting phase. The brine was made from deionized
145 water doped with 25 wt% potassium iodine (KI) as a contrast agent due to its high X-ray
146 attenuation coefficient. This solution provided a strong contrast to identify the fluid phases in the
147 micro-CT images.

148 2.1.2. Drainage experiment

149 The experimental apparatus and flow lines are shown in Figure 2. The rock sample was placed on
150 top of a water-wet ceramic porous plate (Cobra Technologies B.V., NL) and then wrapped in a
151 Viton sleeve. The hydrophilic porous plate had a breakthrough pressure of 1300 kPa to prevent
152 early breakthrough of the non-wetting phase. This assembly was placed in an X-ray transparent
153 flow cell made out of PEEK (RS Systems, Norway), connected to high-precision syringe pumps
154 supplying the experimental fluids. A differential pressure transducer (Keller PD-33X) was
155 connected to the inlet and outlet of the sample. The flow cell was then placed on the Environmental
156 Micro-CT (EMCT) scanner at Ghent University's Centre for X-ray Tomography (UGCT) (Dierick
157 et al., 2014; Bultreys et al., 2016a). This scanner consists of a rotating source-and-detector gantry,
158 meaning the flow cell remained static during the full experiment. Throughout the experiment, the
159 X-ray beam was filtered with 1 mm aluminium to reduce the beam hardening effect. The
160 experiment was performed by executing the following steps:

161

- 162 1. A confining pressure of 3500 kPa was set to compress the Viton sleeve, to avoid fluid
163 bypassing along the wall of sample.
- 164 2. The water-saturated sample was scanned by micro-CT at room temperature and pressure.
165 The imaging settings were: 6.5 μm voxel size, 2400 projections, 1150 ms integration time
166 per radiograph; 110 kV and 8 W X-ray tube settings. Since water has a low grey value
167 similar to air in the images, we will refer to this as the “dry scan” or “dry image” in
168 following sections for convenience.
- 169 3. The water was flushed out by brine, which was injected through the sample with a
170 maximum flow rate of 0.075 ml/min for 4 hours and left overnight. A high-quality micro-
171 CT scan was conducted to capture the sample’s 100% brine saturated state (same imaging
172 settings as step 2).
- 173 4. The drainage was started by injecting decane from the top of the flow cell at a low flow
174 rate (0.001 ml/min). To set a constant pressure drop over the sample, which at vanishing
175 flow rates yields a set capillary pressure in the sample, the flow rate was subsequently
176 gradually lowered based on manual inspection of the pressure transducer reading. This
177 proved to be more reliable than using automated constant-pressure settings on the syringe
178 pump, particularly at low set pressures. The experiment remained capillary dominated at
179 all times during this equilibration procedure, as the maximum capillary number was $6.2 \times$
180 10^{-8} .
- 181 5. Radiographs of the sample were collected and subtracted from each other to track the
182 saturation change in the sample during the equilibration (supporting information Figure
183 S1). In addition, a short micro-CT scan (6.5 μm voxel size, 2400 projections, 115 ms
184 exposure time) was performed every hour to further compare flow distribution changes.
185 When no more changes were found from both the differential radiographs and the
186 subsequent micro-CT images at the target pressure, a high-quality scan (imaging settings
187 see step 2) was taken.
- 188 6. Steps 4 and 5 were repeated with gradually increasing pressure. We performed 6 capillary
189 pressure steps during the experiment, at 8, 14, 80, 180, 220 and 400 kPa. Equilibration took
190 between 4 and 7 hours for the different pressure steps, in all cases having reached very low
191 final flow rates (below 0.0003 ml/min).

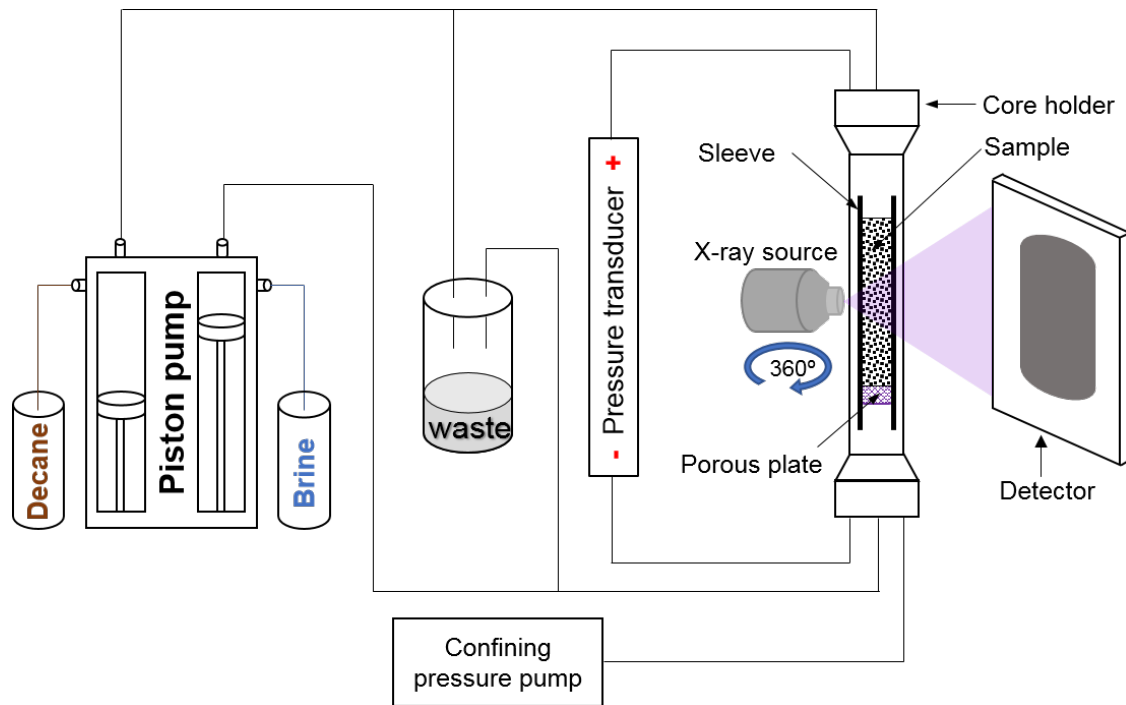


Figure 2. Experimental apparatus used in the drainage experiment.

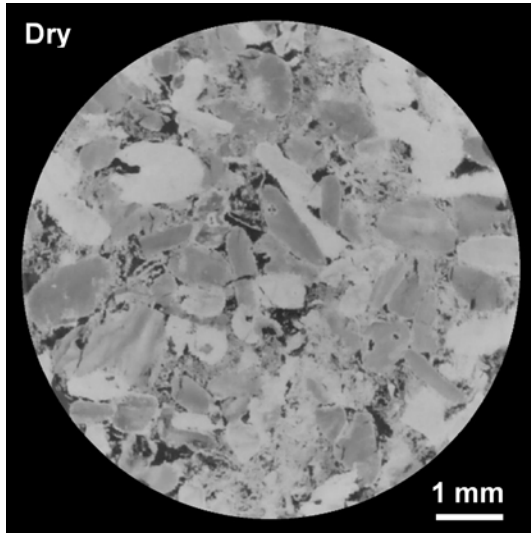
193

194

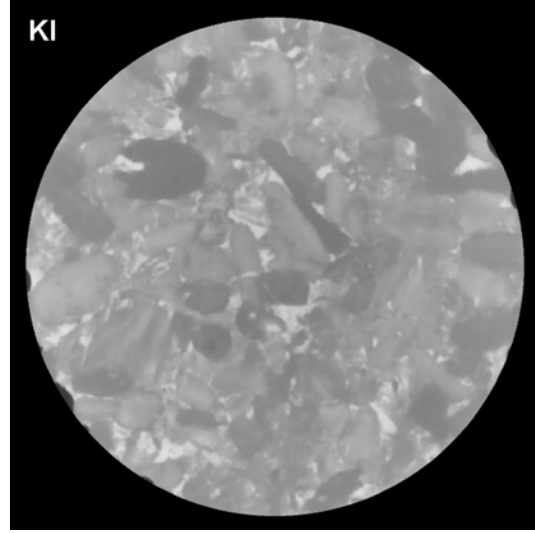
195

196 2.1.3. Micro-CT image processing

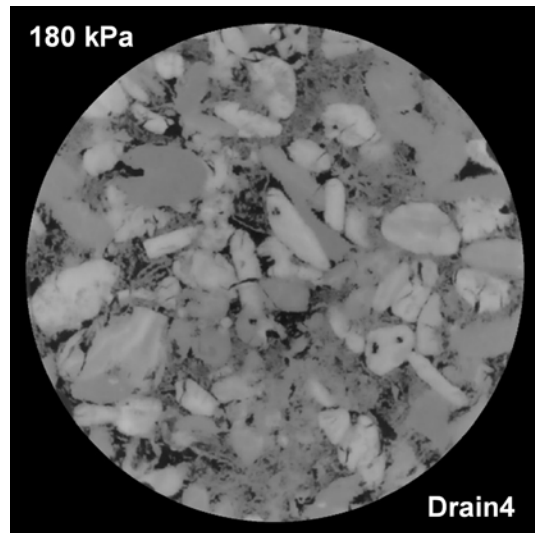
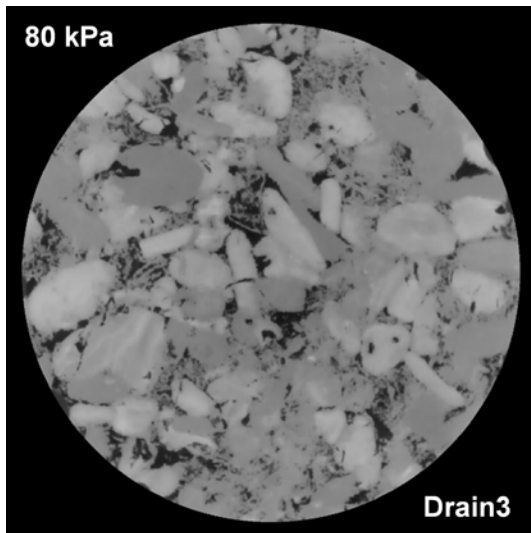
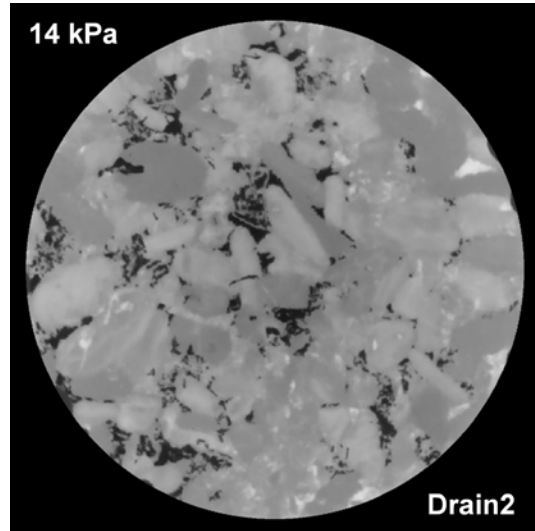
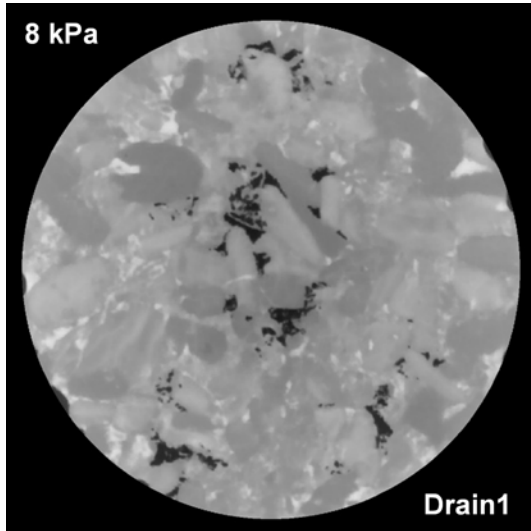
197 The acquired tomograms, which represent the 3D distribution of X-ray attenuation coefficients in
 198 the sample, were reconstructed using Octopus Reconstruction software (Tescan-XRE, Belgium).
 199 After reconstruction, the image processing was performed using Avizo 2020.2 (ThermoFisher,
 200 France). The brine-saturated and drainage-step images were all registered to the dry image using
 201 normalized mutual information and resampled using the Lanczos algorithm to make sure all the
 202 images are aligned in space. The images were then filtered with a non-local means edge-preserving
 203 filter to reduce the image noise. As shown in Figure 3, the pores in the dry scan image are dark
 204 grey and have significantly lower grey values than solid calcite grains. In the brine-saturated image,
 205 the brine-invaded pores are brighter than other phases in the sample. A cross-section of the fluid
 206 distribution in the 6 capillary pressure steps is shown in Figure 3(c). With the increase of drainage
 207 pressure, the brine is displaced by decane, and brighter pores gradually become “black”.

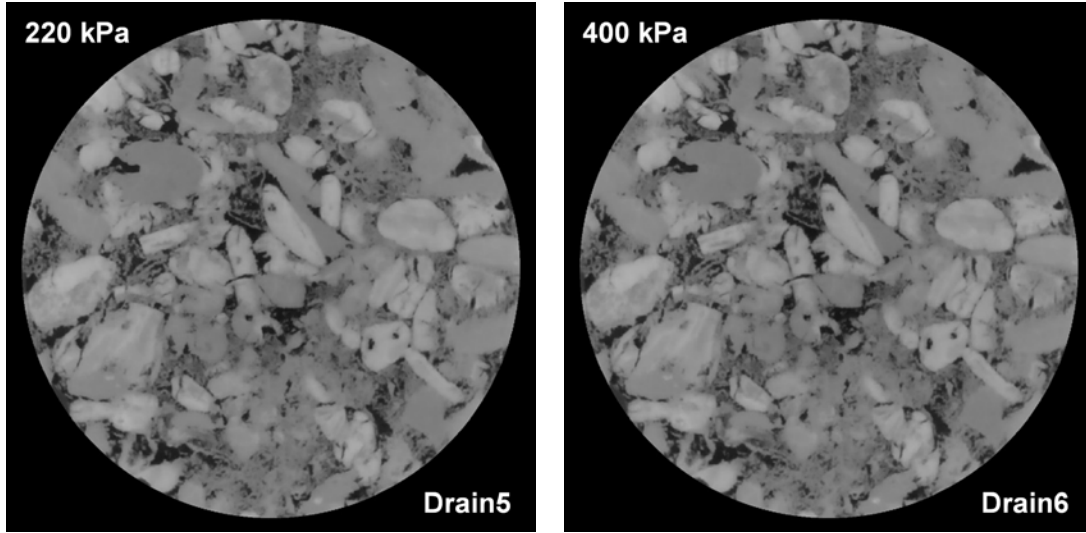


(a)



(b)





(c)

208 Figure 3. (a) Dry san. (b) KI saturated scan. (c) Drainage scans at 6 capillary pressures.

209

210 Although the KI-brine visually already indicates the presence of different fluid phases within
 211 macropores, further processing is necessary to quantify the brine saturation in the unresolved
 212 porosity. We propose an improved workflow here based on differential imaging with normalized
 213 water-filled and brine-filled images to calculate the sub-resolution saturation in voxels that contain
 214 microporosity.

215 The image normalization is based on selecting fixed grey values for two known materials, setting
 216 them to the same value in the different images, and doing a linear rescaling of everything in
 217 between. To normalize the brine-saturated image to the dry image, we first cropped 3 region-of-
 218 interests (ROI) of solid grain to determine the upper normalization value, and an ROI in the sleeve
 219 (which has a low grey value) for the lower value. The rescaled image was calculated following
 220 equation (1), which is adapted from Lin et al, (2017):

$$221 \quad I_{new} = (I - p_{s_brine}) \cdot \frac{p_{g_dry} - p_{s_dry}}{p_{g_brine} - p_{s_brine}} + p_{s_dry} \quad (1)$$

222 Where I_{new} is the rescaled image, I is the image before normalization, p_{g_dry} is the average mode of
 223 the 3 solid grain ROIs from the dry image, p_{s_dry} is the mode of the grey value histogram of the
 224 sleeve ROI from the dry image, p_{g_brine} is the average mode of the 3 solid grain ROIs from the
 225 brine saturated image, and p_{s_brine} is the mode of the sleeve ROI from the brine saturated image.

226 For the drainage images, we first cropped 3 ROIs in solid grains and 3 ROIs in water-filled resolved
 227 pores from the dry and the 6 drainage images, extracted their grey value histograms and calculated
 228 their modes. The drainage images were then rescaled according to equation (2):

$$229 \quad I_{new} = (I - p_{d_drain}) \cdot \frac{p_{g_dry} - p_{w_dry}}{p_{g_drain} - p_{d_drain}} + p_{w_dry} \quad (2)$$

230 Where p_{g_dry} is the average mode of 3 solid grain ROIs in the dry image, p_{w_dry} is the average mode
 231 of 3 water-invaded-pore ROIs from the dry image, p_{g_drain} is the average mode of 3 solid grain
 232 ROIs from the drainage images, p_{d_drain} is the average mode of 3 decane-invaded-pore ROIs from
 233 drainage images.

234 Then, the differential image was obtained by calculating the differences between the rescaled
 235 drainage- or brine saturated images and the water-filled image:

$$236 \quad I_{diff_drain} = I_{new_drain} - I_{dry} \quad (3)$$

$$237 \quad I_{diff_brine} = I_{new_brine} - I_{dry} \quad (4)$$

238 The dry-brine differential image was used to quantify sub-resolution porosity in the image, due to
 239 the assumed linear dependence of the grey value in the differential image and the volume
 240 percentage of brine present in each voxel. We denote the thresholds set for solid (0% porous) and
 241 open porosity (100% porous) voxels as CT1 and CT2, respectively. CT1 was determined based on
 242 the valley between the grey value distributions of the solid and microporous phase in the histogram.
 243 CT2 was found by masking the differential image with the macropores segmented from the dry
 244 image, and finding the peak of the associated grey value histogram (supporting information Figure
 245 S2). Voxels with grey values equal to or less than CT1 are assigned 0% porosity, those equal to or
 246 higher than CT2 are assigned 100% porosity, the microporous region between CT1 and CT2 is
 247 assigned 0~100% porosity, using:

$$248 \quad \varphi_{micro} = \frac{I_{diff_brine} - CT1}{CT2 - CT1} \quad (5)$$

249 Where φ_{micro} is the porosity within microporous voxels. The total porosity can be calculated by:

$$251 \quad \varphi_{total} = \frac{V_{macro} + V_{micro} * \varphi_{micro}}{V_{sample}} \quad (6)$$

252 Where V_{macro} is the number of macropore voxels, V_{micro} is the number of micro-pore voxels, V_{sample}
 253 is the number of voxels in the whole sample.

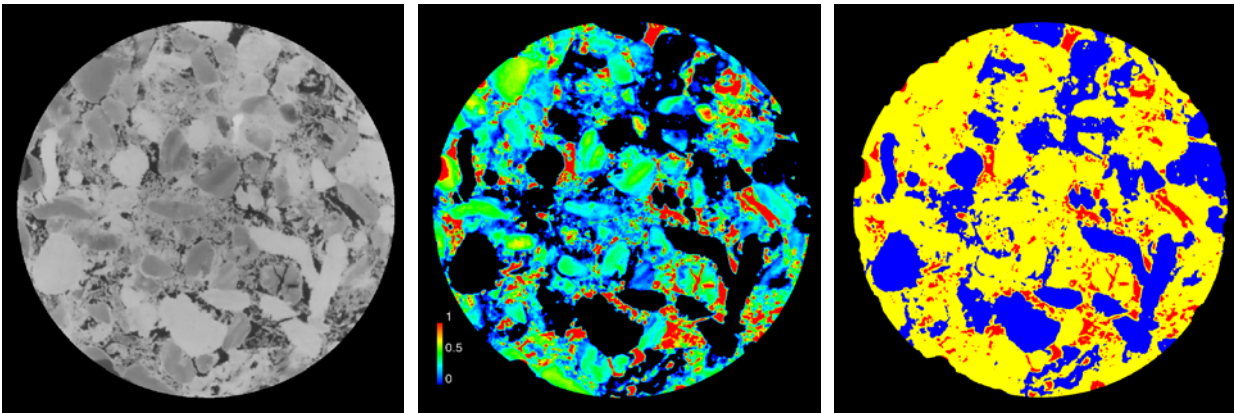
254 Similarly to the porosity map, we also calculated the brine saturation map at each capillary pressure
 255 step using the equation (7):

256

$$S_{w_drain} = \frac{\varphi_{drain}}{\varphi_{micro}} = \frac{I_{diff_drain} - CT1}{I_{diff_brine} - CT1} \quad (7)$$

257 With this method, the porosity distribution map was obtained, shown in Figure 4(b), which
 258 provided a 3D distribution of the porosity variation within the microporous phase. Table 1 shows
 259 the porosity calculation results. The total porosity of this sample was 25.43%, of which the sub-
 260 resolution porous regions contributed 78.53%. The 3 components, macropores, microporous
 261 regions and solid grains, were extracted from this porosity map (Figure 4(c) and supporting
 262 information Figure S3).

263



264

(a)

(b)

(c)

265

266 Figure 4. Porosity distribution map. (a) A slice from the filtered dry image (b) The corresponding porosity
 267 distribution map at the same slice (c) Three-phase segmentation of the sample into macropores (red),
 268 microporous regions (yellow) and solid (blue).

269

270

Table 1. Porosity calculation

Phase	Threshold	Voxel ($\times 10^8$)	Voxel*Porosity ($\times 10^8$)	Average porosity	Volume fraction	Contribution	Total porosity
macro	>1	0.42576		1	0.05463	0.05463	
micro	0-1	5.01773	1.55637	0.31017	0.64381	0.19969	0.2543
grain	<0	2.35033		0	0.30156	0	

271

272 2.2 Multi-scale model

273 2.2.1 Sub-rock typing

274 Multi-scale models of multiphase flow depend on the classification of regions with sub-resolution
 275 porosity. To identify these regions, and inform their description in the model, a recently proposed
 276 method is to segment a sub-resolution porosity map of the sample into different “sub-rock types”.
 277 We will refer to this as the “porosity-based” method. A crucial first step is to generate an accurate
 278 porosity map (Figure 4(b)). Figure S4 in supporting information depicts the histogram of the
 279 porosity distribution in the sample. Two thresholds (0.2 and 0.4) were manually selected to divide
 280 the sample into 3 microphase regions or 3 rock types (3RT), based on trial-and-error to obtain
 281 realistic simulation results for the capillary pressure curve (see further). The sub-rock typing result
 282 is shown in Figure 6.

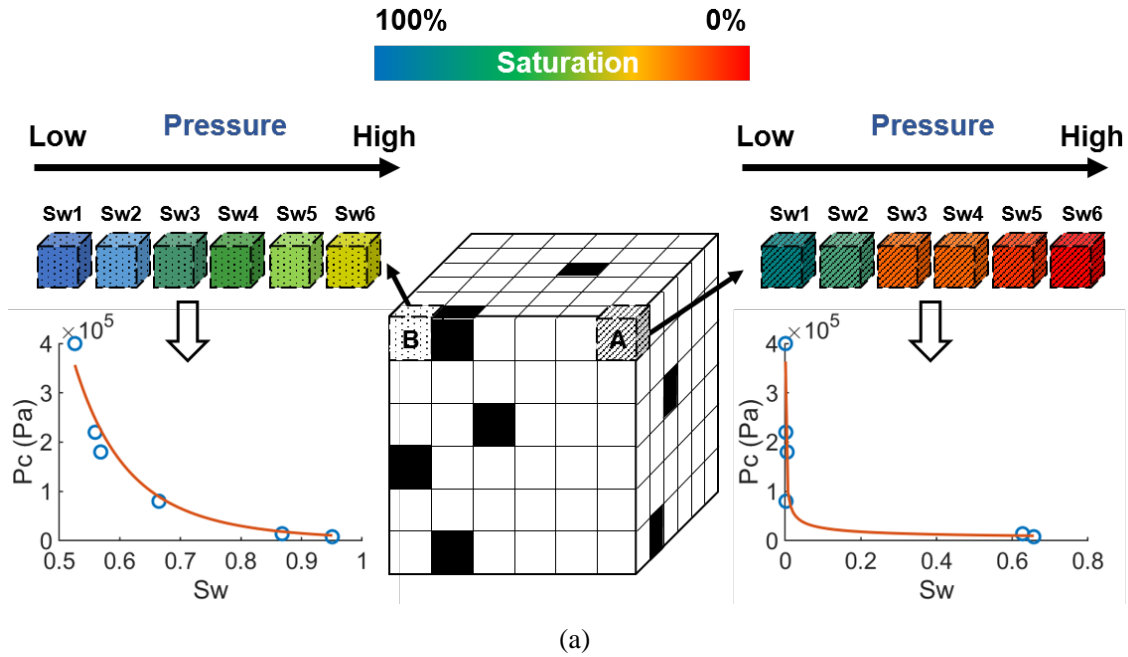
283 The downside of porosity-based sub-rock typing is that it is based on the assumption that porosity
 284 is closely correlated to the multiphase flow properties of the microporosity. This is not necessarily
 285 the case. Therefore, we introduce a new method here to perform rock typing based directly on
 286 experimental multiphase flow data. To this end, we determined the invasion capillary pressure (P_{ct})
 287 distribution within the microporous phase. First, the saturation map at each drainage pressure step
 288 was calculated (Section 2.1.3). The saturation variation with the increase of pressure of every
 289 individual voxel was thus obtained. Next, these saturation maps were mean-filtered and
 290 downsampled by a factor 2 to reduce the noise dependency and computational load. Then, a
 291 Brooks-Corey-type P_c formulation (Brooks & Corey, 1964) was fitted to the capillary pressure-
 292 saturation data points of each voxel using a least-squares approach in Matlab. This yielded a
 293 relation of the following form for each voxel:

$$294 \quad P_c = P_{ct} \left(\frac{1}{S_w} \right)^{\frac{1}{\lambda}} \quad (8)$$

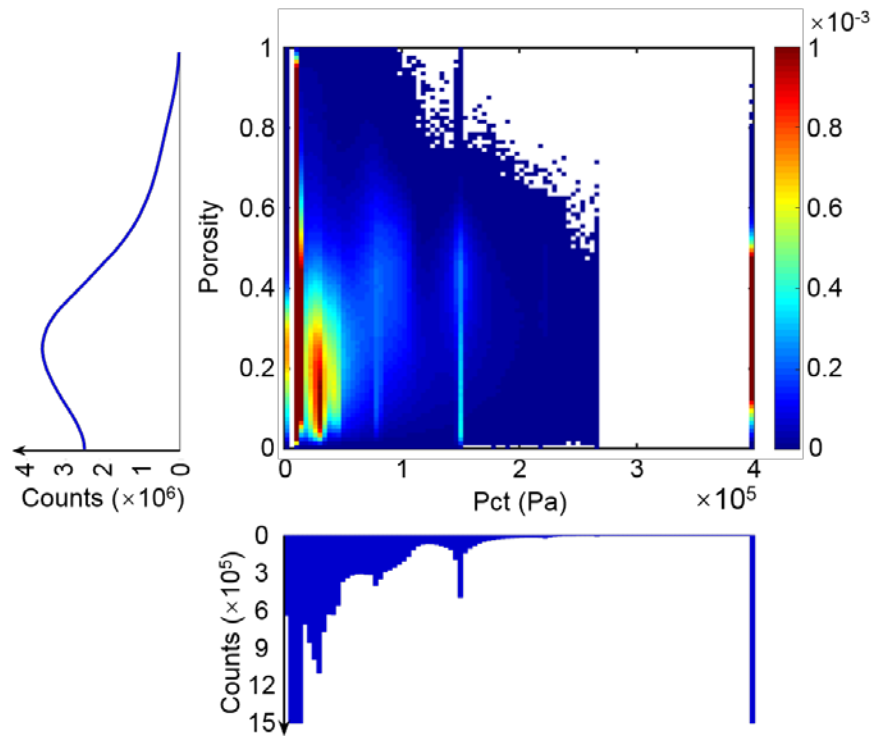
295 Where P_c is the capillary pressure, P_{ct} is the fitted invasion capillary pressure, λ is a fitted parameter
 296 related to the pore size distribution and S_w is water saturation.

297 In this way, P_{ct} and λ values were derived for all microporous voxels. The fitted curves for two
 298 representative voxels are shown in Figure 5(a). Figure 5(c) presents the P_{ct} map and the λ map,
 299 showing the 3D variation of the capillary pressure behavior in the sample. We primarily used the
 300 P_{ct} map here due to its easier interpretability and lower noisiness than the λ -map. We considered

301 both porosity and P_{ct} together by performing a k-means clustering on the (ϕ, P_{ct}) points of all the
 302 voxels (Figure 5(b)). This was used to divide the voxels into 5 clusters, representing 5 microporous
 303 subrock types, next to the microporous and solid voxels in the image.



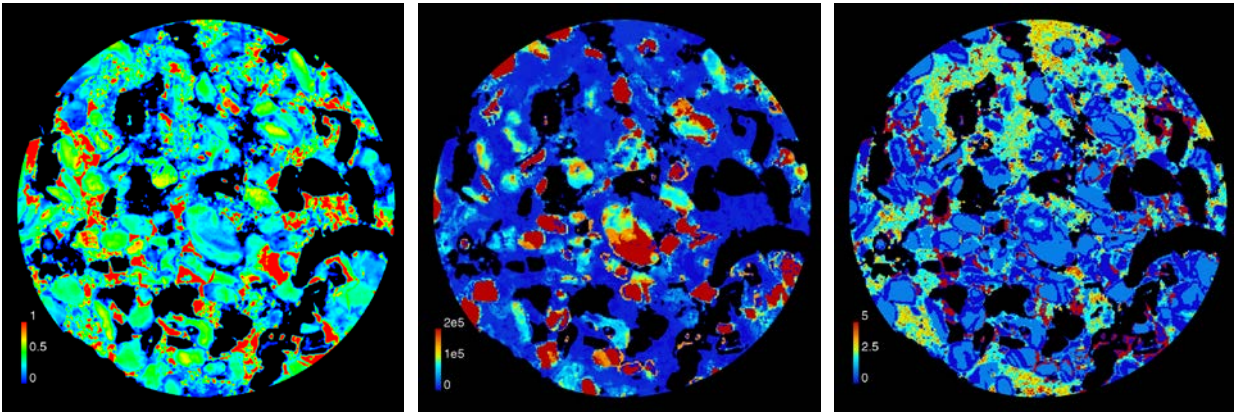
304
 305
 306



307
 308

(b)

309



(c)

310

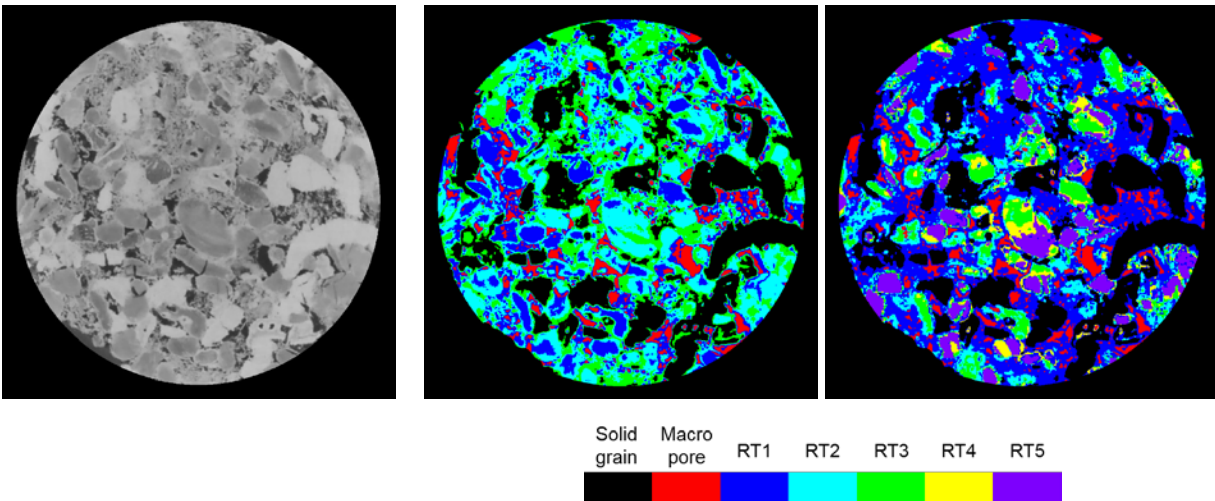
311 Figure 5. Pct-based sub-rock typing workflow. (a) The diagram of data fitting of two representative voxels. (b)
 312 A plot of Pct versus porosity. (c) Porosity map (left), Pct distribution map (middle) and λ distribution map (right).

313

314 2.2.2 Pore network extraction and simulations

315 Two multi-scale PNMs of the sample were extracted using the porosity map and the sub-rock type
 316 maps as input. These PNMs consist of four types of network elements: resolved nodes (“pores”)
 317 and links (“throats”) that represent the macroporosity and unresolved (“Darcy”) nodes and links
 318 that represent the microporosity. The extraction is based on skeletonization and maximal ball
 319 clustering of the resolved pore space and each of the microporosity sub-rock types in order to find
 320 the centers of nodes and links, as described in Øren et al. (2019). These are then connected together
 321 to honour the connectivity of the multi-scale pore-space. Geometrical properties (e.g. inscribed
 322 radius, volume, shape factor) of the network elements are subsequently determined. For Darcy
 323 nodes and links, the geometrical properties are supplemented by the local porosity determined
 324 from the porosity map, and local petrophysical properties based on user input for each sub-rock
 325 type (see Section 2.2.3). Full details on the method can be found in Ruspini et al. (2021). We
 326 extracted two different PNMs of the same sample, based on respectively the porosity-based sub-
 327 rock typing map and the Pct-based sub-rock typing map (Figure 6). The properties of these PNMs
 328 are shown in Table 2. The total porosity was 26.2% with 5.6% contributed by macropores and
 329 20.6% by micropores, which honours the micro-CT results (Table 1).

330



331 Figure 6. Dry image (left), porosity-based sub-rock typing result (middle) and Pct-based sub-rock typing result
 332 (right). The red and black in both sub-rock typing maps refer to macropores and solid grain. In porosity-based
 333 map: RT1, RT2 and RT3 show high, middle and low microporosity regions respectively. In Pct-based map: RT1
 334 to RT5 represent lower to higher Pct microporous regions.

335

336 After extraction, the resulting PNMs were used to predict permeability and pore-scale fluid
 337 distributions during drainage. Permeabilities were calculated by assigning a conductivity value to
 338 each element (based on Poisseuille flow in resolved network elements and Darcy's law in Darcy
 339 elements, taking the local microporosity's permeability) and solving a set of mass balance
 340 equations (Ruspini et al., 2021). Drainage was simulated quasi-statically by calculating an
 341 intrusion capillary pressure for each network element, and then performing an invasion-percolation
 342 (i.e. progressively invading accessible network elements in ascending order of their intrusion
 343 capillary pressure). Invasion capillary pressures for resolved pores and throats were calculated by
 344 assuming triangular, square or cylindrical cross-sectional shapes (Mason & Morrow, 1991). In
 345 Darcy elements, the invasion pressure was found from input capillary pressure curves of the sub-
 346 rock type (scaled according to the local porosity and permeability using the Leverett-J-curve). The
 347 simulation took fluid connectivity through wetting layers into account, and assumed a fluid to be
 348 connected through a Darcy element as long as the local relative permeability to the fluid was larger
 349 than zero. Full details are provided in Ruspini et al. (2021).

350

351

352

Table 2. Properties of extracted PNMs

Properties	Porosity-based model	Pct-based model
Nodes	666543	658120
Links	4334582	5006058
Darcy pore	4898310	5561272
Total porosity	0.2625	0.2624
Resolved porosity	0.0564	0.0563
Unresolved porosity	0.2061	0.2061

353

354 2.2.3 Petrophysical properties

355 The petrophysical properties taken into account to represent unresolved porosity in each Darcy
356 node of the PNM are porosity, permeability, relative permeability and capillary pressure curve (P_c -
357 curve). The local porosity in each element was determined from the porosity map. Compared with
358 the traditional way of assigning an average porosity value to the whole microporosity phase, the
359 introduction of the porosity map captures more realistic porosity heterogeneity. The permeability
360 for each node was calculated from a power correlation $k = a * \varphi^b$, where a and b are supplied as
361 input values for each sub-rock type. Parameter b was set to 3.37 for all types based on a nm-scale
362 imaging study performed by Menke et al. (2019) on microporosity in Estaillasses. Since the
363 microporosity's permeability values affect the intrusion capillary pressure curve of Darcy nodes
364 through Leverett-J scaling, parameter “a” was tuned to match the output P_c -curve of the PNM
365 simulations with our experimental P_c -curve measurement (Section 2.1). Note that anchoring
366 simulations to available experimental data is common practice for multi-scale models, in order to
367 allow better predictions of more difficult-to-obtain properties.

368 The determination of the relative permeability curve for each rock type is a challenging task, as
369 this property is difficult to measure directly. Here, the Brooks-Corey model (Brooks & Corey,
370 1966) was used to assign the same relative permeability curves to all Darcy elements, in order to
371 decrease its uncertain influence on the drainage simulation results. Approaches to obtain more
372 accurate relative permeability curves for different micro-regions are the subject of future
373 investigations.

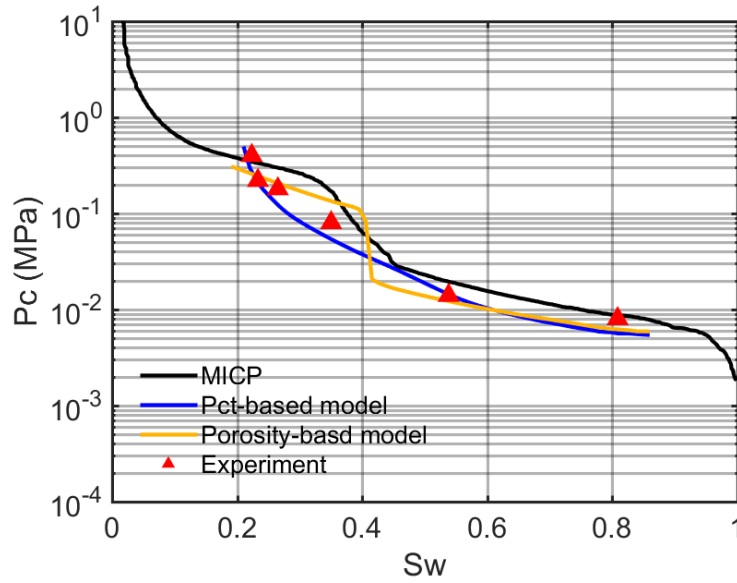
374 For the porosity-based PNM, the Brooks-Corey-type P_c formulation (Brooks & Corey, 1964) was
375 fitted to the experimental P_c -measurement to obtain P_c -curves for each microporosity type. The
376 fitted curve was split into three parts, corresponding to the three microporosity regions from the
377 porosity map (see Section 2.2.1). The saturation range of each of these parts was then rescaled to

378 a range between 0 and 1, to serve as input P_c -curves for the sub-rock types, where the curve with
379 the lowest P_c -range was assigned to the rock type with the highest porosity. Note that this
380 workflow represents a coarse fit of the input properties to the experimental P_c -data (see e.g.
381 Bultreys et al. 2015), but that this may not generally yield good results for all samples, and that
382 there is no set way to divide the experimental P_c -curve into the individual sections (in this work,
383 this was done by trial-and-error, until a satisfactory fit was found between the simulated and the
384 experimental P_c -curves). For the Pct-based PNM, the input P_c -curves of each rock type were
385 calculated directly from the imaging data, that is, the average saturation within each sub-rock type
386 was determined at each capillary pressure step. This significantly reduced the input uncertainty of
387 the simulations compared to the porosity-based workflow.

388 **3 Results**

389 3.1 Simulation results

390 The permeability values simulated with the Pct-based model and porosity-based model were 69.93
391 mD and 9.54 mD respectively, compared to literature values of 95.5 mD to 283.6 mD (Alyafei et
392 al., 2015; Bultreys et al., 2015; Nono et al., 2014) and minipermeameter values 202.4 ± 86.9 mD.
393 To validate the experimental workflow and the image analysis results from it, we compared the
394 drainage results with a capillary pressure curve obtained using mercury intrusion capillary pressure
395 (MICP) method (Bultreys et al., 2015), rescaled to the water-decane interfacial tension (48.3 mN/m)
396 and contact angle (0°). As shown in Figure 7, the evolution of the saturation from the imaging with
397 the capillary pressure imposed in our experiment agreed well with the MICP data, indicating that
398 the experimental operation and data processing methods were reasonable and reliable. Furthermore,
399 the simulated capillary pressure curves also showed a good match with our experiment, and the
400 input parameters were thus considered to be reasonable for the further pore-by-pore evaluation of
401 the model.
402



403

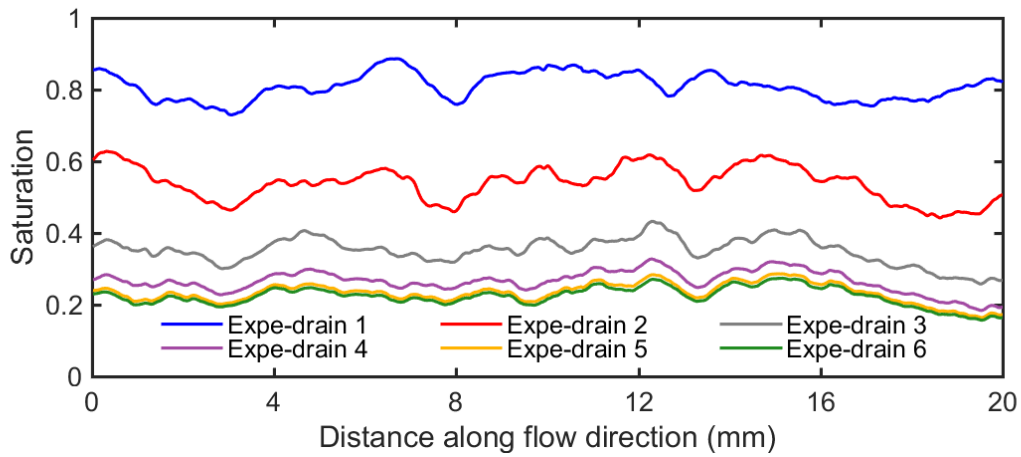
404 Figure 7. Comparison of capillary pressure curve obtain from MICP experiment, our drainage experiment, and
 405 simulations.

406

407 3.2 Model validation of fluid distributions

408 Figure 8 shows the slice-average profile of the brine saturation along the flow direction in the
 409 sample. Visual comparison indicates that the distribution simulated by the Pct-based model
 410 generally fits more closely to the experimental measurements.

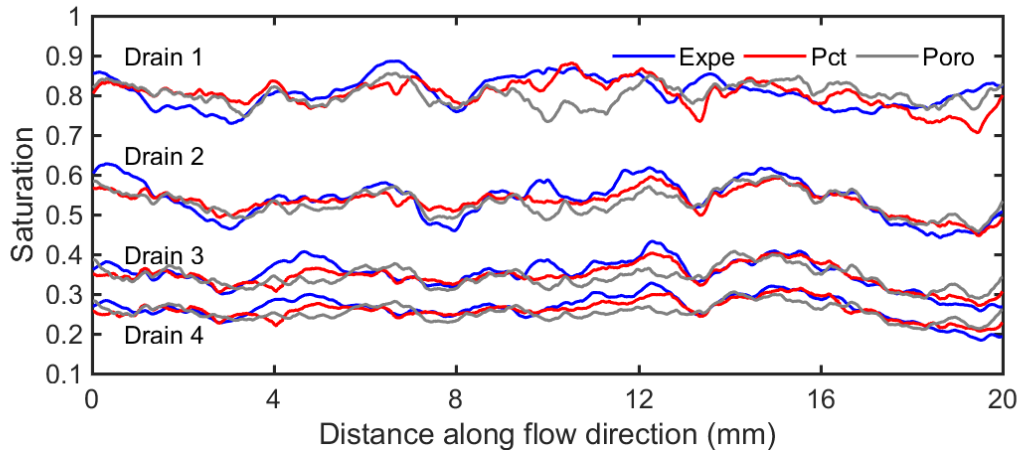
411



412

413

(a)



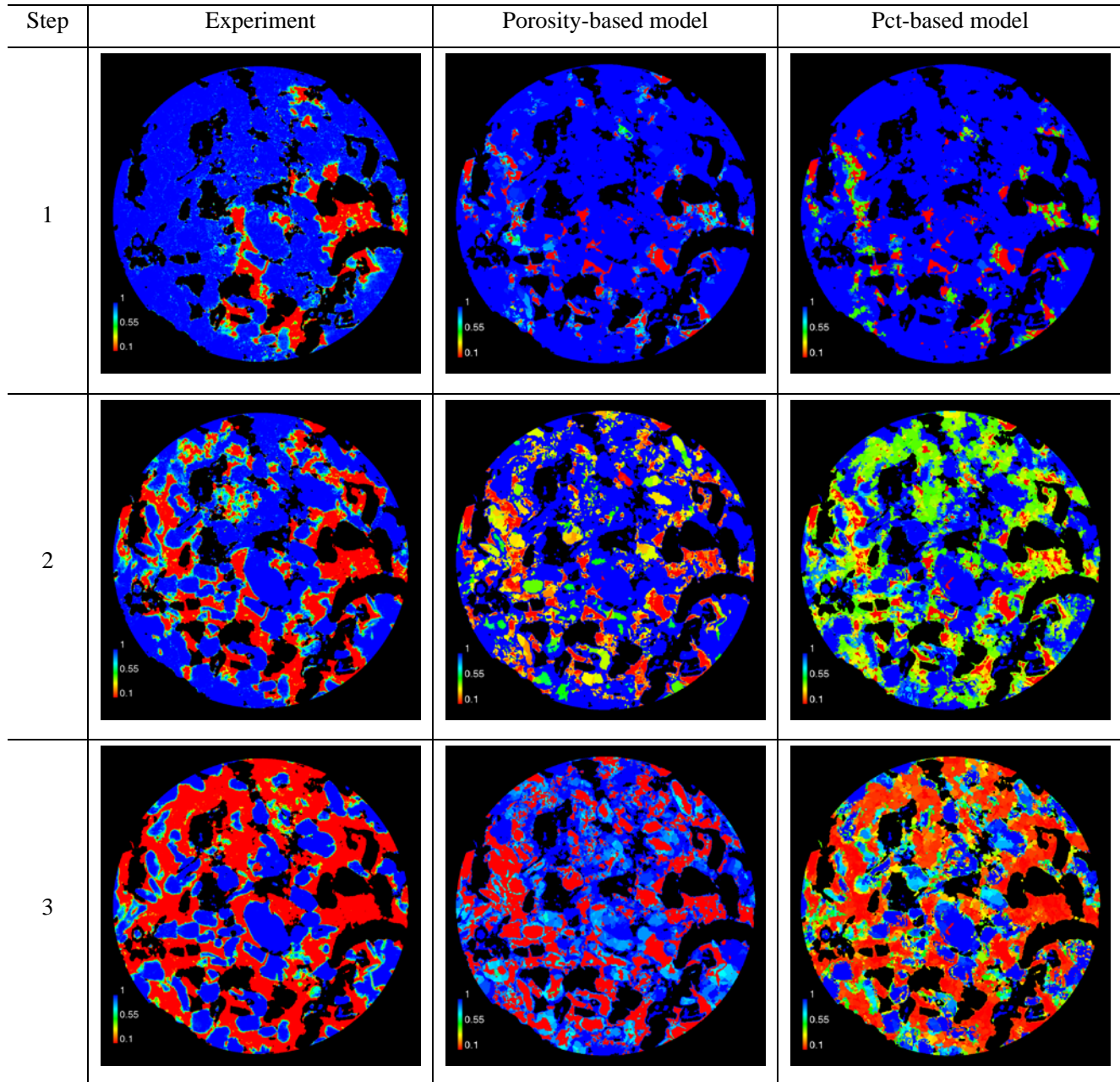
(b)

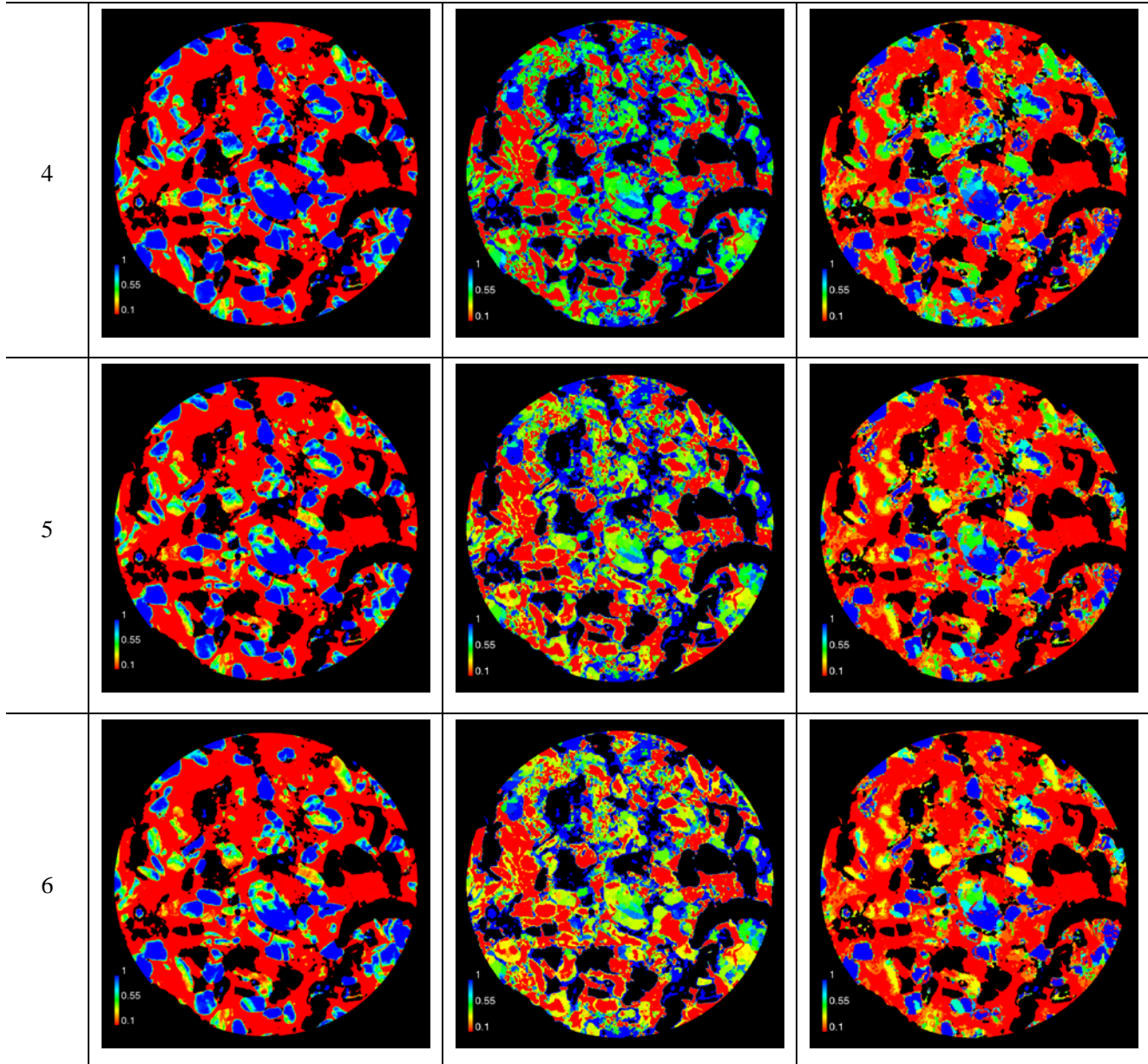
414
 415
 416 Figure 8. Brine saturation slice-average profiles along fluid flow direction. (a) Experimental results. (b)
 417 Comparison of experiment and model predictions at 1 to 4 drainage steps.

418
 419 The simulations were then compared to each step of the imaging experiment at a matching total
 420 saturation. Figure 9 shows the comparison between saturation distributions of the experiment and
 421 the two model cases. In the first and second drainage stage, due to the low capillary pressure, large
 422 macro pores and well connected micropores are invaded by oil, while other macro pores remain
 423 uninvaded or partially invaded. From the third capillary pressure on, the displacement takes place
 424 almost completely in the microporous regions. This general trend was captured by both models.
 425 However, visual inspection of the fluid saturation maps shows that the new Pct-based model
 426 performs significantly better than the classical porosity-based model in predicting the fluid
 427 distribution.

428 The observed discrepancy in the porosity-based model is related to the fact that the porosity-based
 429 model (similarly to most classical multi-scale models) assumes that regions with higher porosity
 430 have larger pore sizes and are more easily drained. Contrary to this classical assumption, the
 431 experiment shows that the sub-rock type with the lowest average porosity has the lowest water
 432 saturation at high capillary pressure steps (Figure 10). While the model contained enough degrees
 433 of freedom for it to be tuned to the sample-averaged capillary pressure curve in Figure 7, this is
 434 not the case for the pore-scale distribution of the fluids. Matching this distribution is known to be
 435 a crucial issue to obtain reliable relative permeability curves from the model (Bultreys et al., 2020;
 436 Gharbi & Blunt, 2012; Ruspini et al., 2017). Comparison to the novel Pct-based method, which is

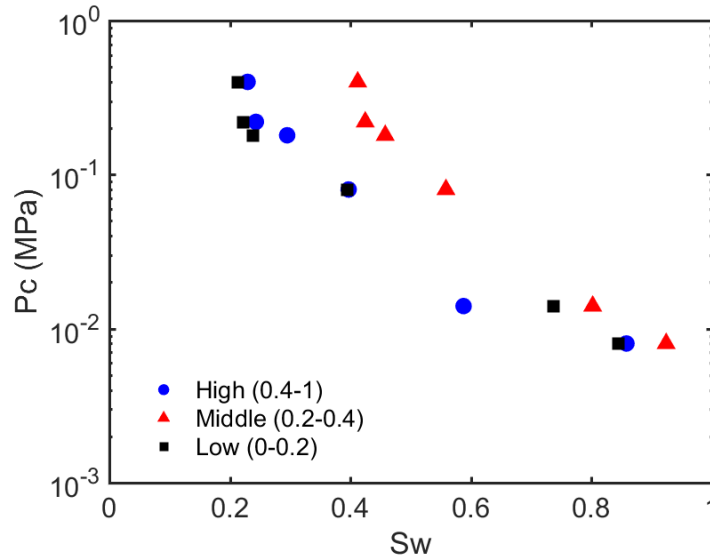
437 directly based on the breakthrough pressure of each pore and provides a much better match, shows
 438 that the fluid distribution discrepancy can be resolved by avoiding the basic assumption that higher
 439 porosities are related to lower intrusion capillary pressures in the sub-rock typing.
 440





441 Figure 9. Saturation map comparison at each drainage pressure. The left column is experimental results. The
 442 middle and right column are simulation results in porosity-based and Pct-based pore network model.

443



444

445 Figure 10. Average experimental saturation for the 3 micro-phase regions determined by the porosity-based sub-
 446 rock typing, for each capillary pressure step. These are the high (0.4-1), middle (0.2-0.4) and low (0-0.2) porosity
 447 regions respectively.

448

449 3.3 Saturation error

450 To investigate the accuracy of the predicted saturations further, we compared the simulations to
 451 the experiment directly on the image by calculating the squared saturation error in each voxel:

452 $(S_{w_exp} - S_{w_mod})^2$. Cross-sections of these saturation error maps are shown in Figure 11(a).

453 The Pct-based model generally shows higher accuracy than the porosity-based model, especially
 454 unresolved regions at high capillary pressures.

455 The saturation error in certain open pores and in pores just above the image resolution is relatively
 456 large in the beginning of drainage in both models (pressure steps 1-3). To explain this, Figure 12

457 shows the pore radius distribution of water filled macropores and throats in the experiment and in
 458 the Pct-based model. We define the discrepancy of the filling state as the percentage of network

459 elements that were occupied by a different fluid in the simulation than in the experiment (Bultreys
 460 et al., 2018). If more than half of the fluid within a single pore or throat was wetting phase, the

461 pores or throats were considered to be wetting phase occupied, otherwise, they were classified as

462 non-wetting phase filled. As expected, the non-wetting phase invaded large open pores and throats

463 in the beginning, and almost all the brine within them was displaced before increasing to the fourth

464 pressure. Similar to single-scale models (Bultreys et al., 2018), the pores and throats with
 465 intermediate size had the largest filling discrepancy. At the first drainage pressure, the occupancy
 466 for pores with large radius ($>12 \mu\text{m}$) had a close match. However, the simulation predicted that all
 467 small pores were wetting-filled while the experiment did not show this behaviour. The throat filling
 468 error also reached 18.14% in this step. As shown in previous studies (Bultreys et al., 2018), the
 469 experimental fluid distribution and filling states at the pore scale are generally not fully
 470 reproducible, even in repeated experiments. Some of the pore-by-pore errors are likely caused by
 471 wrong intrusion pressure predictions in throats that are only just above the resolution. Furthermore,
 472 we only imaged the central part of the sample and the boundary conditions are therefore not exactly
 473 the same in the model and the experiment, which increased the pore-by-pore uncertainty of the
 474 simulation.

475 To quantitatively compare the saturation errors at each drainage step, we calculated the absolute
 476 average root mean square error (δ_{Abs}) and the volume weighted average root mean square error
 477 (δ_{VolWei}) of the models over the entire image:

$$478 \quad \delta_{Abs} = \sqrt{\frac{\sum (S_{w_exp} - S_{w_mod})^2}{N}} \quad (9)$$

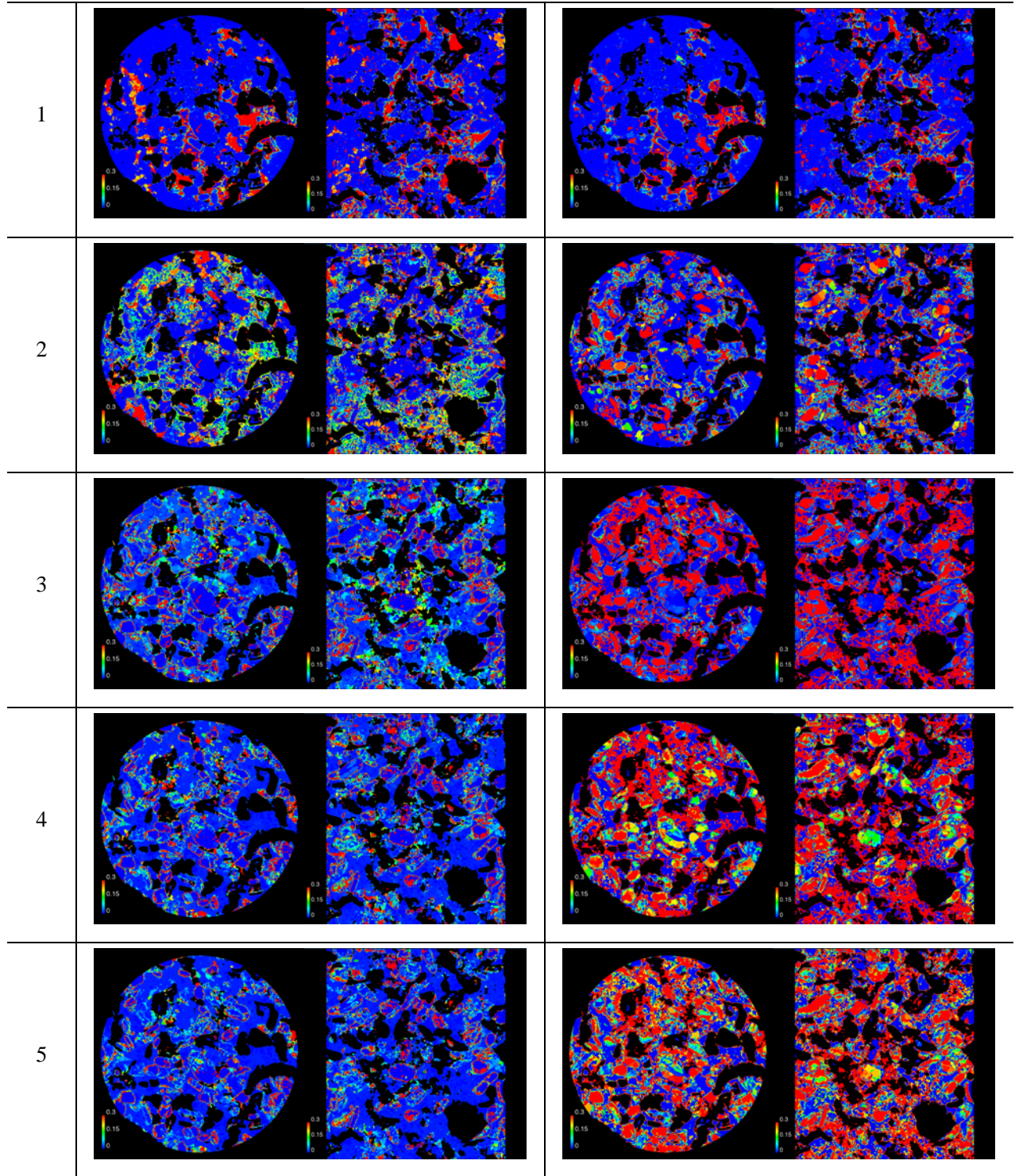
$$479 \quad \delta_{VolWei} = \sqrt{\frac{\sum ((S_{w_exp} - S_{w_mod}) \cdot \varphi)^2}{N}} \quad (10)$$

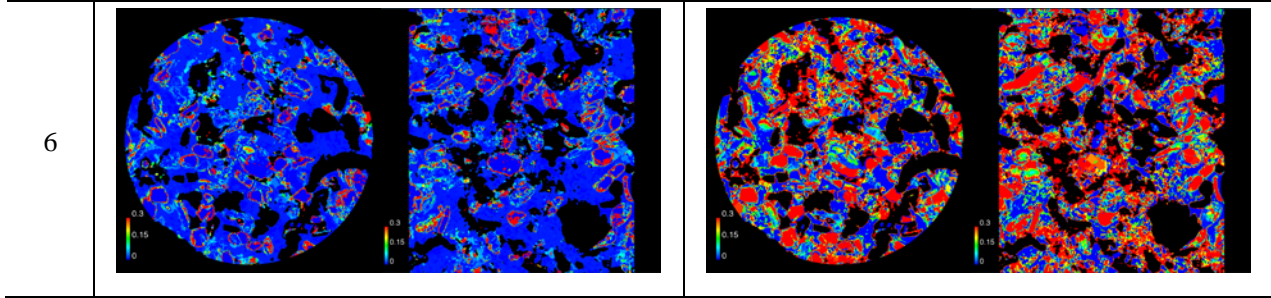
480 Where S_{w_exp} and S_{w_mod} are brine saturation of each voxel from experimental measurements and
 481 simulations respectively, φ is the corresponding porosity of each voxel, N is the total number of
 482 pore voxels.

483 Figure 11(b) indicates that the saturation error in the porosity-based model at high drainage
 484 pressures is significantly higher than that at low pressures, while the Pct-based model shows a
 485 smoother trend and lower errors, decreasing from 0.34 to 0.26 with the increase of pressures. The
 486 volume-weighted error in the porosity-based model is almost twice as high as in the Pct-based
 487 model in drainage steps 3 to 6.

488

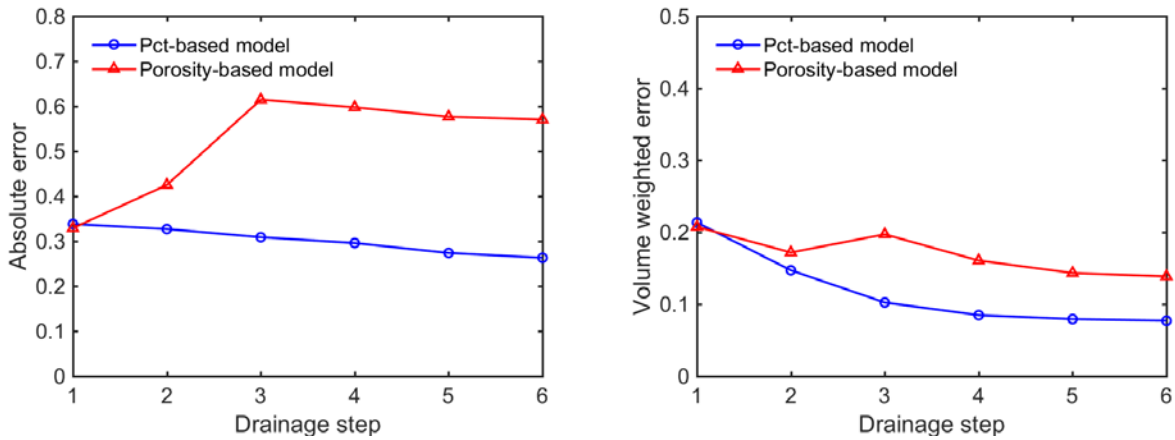
Step	Pct-based model error map		Porosity-based model error map	
	X-Y plane	X-Z plane	X-Y plane	X-Z plane





489

(a)

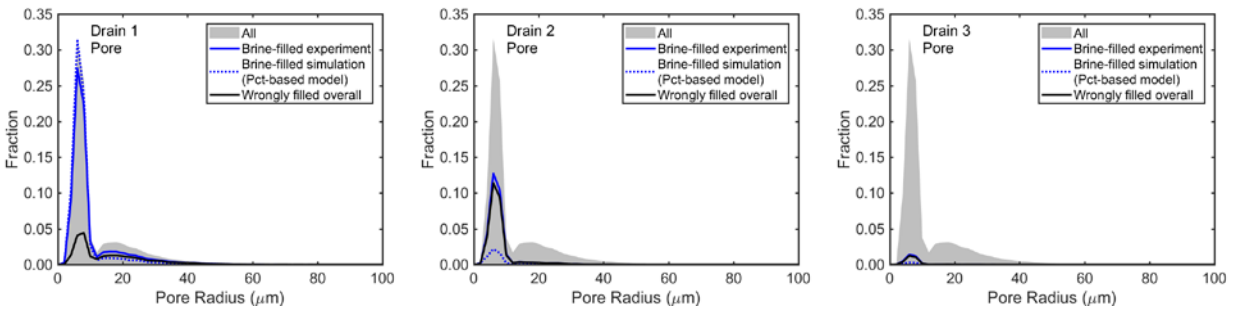


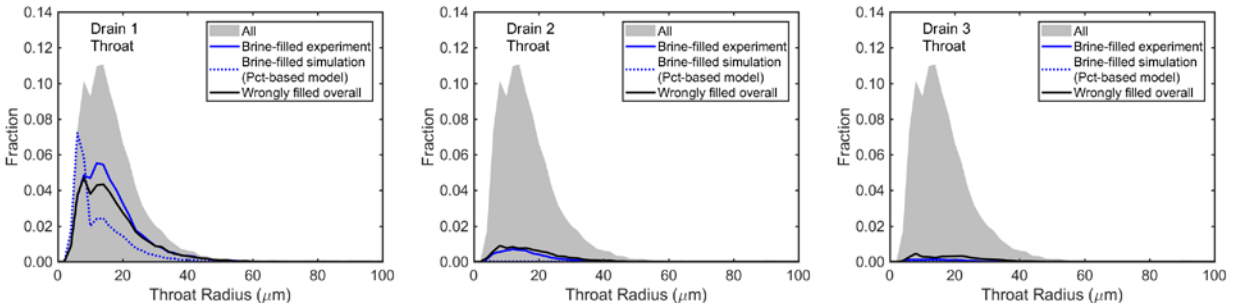
490

(b)

491 Figure 11. Saturation error. (a) Saturation error map. The left two columns (X-Y plane and X-Z plane maps
 492 respectively) are saturation discrepancy between experiment and Pct-based model simulations. The right two
 493 columns (X-Y plane and X-Z plane maps respectively) are saturation discrepancy between experiment and
 494 porosity-based model simulations. The black is solid grain. The blue color represents the simulated saturation
 495 error is very small, while the red color denotes the error is large. (b) Absolute saturation error (left) and
 496 volume weighted saturation error (right) predicted by the two models.

497





498 Figure 12. Water-filled open pore (top) and throat (bottom) size distribution after each drainage step.

499

500 4 Conclusions

501 In this work, we proposed a multi-scale PNM validation workflow using drainage experiments
 502 imaged with micro-CT, to study the factors that influence the uncertainty of pore-scale modelling
 503 and simulation. The differential imaging technique was used to quantify the porosity map and the
 504 saturation distribution during capillary-dominated drainage in an Estailades limestone sample. A
 505 “classical” porosity-based and a novel invasion-capillary-pressure-based sub-rock typing methods
 506 were used to characterize the microporosity, followed by a multi-scale PNM extraction. The
 507 continuum scale properties and pore-scale multiphase distribution from the two models were then
 508 compared to experimental data.

509 We showed that the P_c -curves simulated by both models matched our image-based capillary
 510 pressure curve and an MICP curve of the rock type. The porosity-based model performed poorly
 511 in simulating multiphase fluid distribution at the pore-scale, while the novel Pct-based model
 512 significantly improved the prediction of pore filling states. This indicated that the multiphase
 513 transport behavior within sub-resolution pores was poorly correlated to the sub-voxel porosity.
 514 Further research should indicate if this is due to micropore geometry variations or due to dynamic
 515 effects inside the microporosity, e.g. inhomogeneous drainage due to extremely low brine
 516 conductivities that slow down the invasion to very long time scales. The methodology presented
 517 in this work was proven to be a robust approach in decreasing the uncertainty of pore-scale
 518 modelling and can be extended to other complex reservoir rocks modelling, to provide more
 519 insights on, for example, CO₂ sequestration and reservoir management.

520 Despite the improved results obtained with the Pct-based method, the determination of input
 521 petrophysical properties for microporous flow zones is still challenging and was shown to be a key

522 factor affecting the reliability of the simulation. Furthermore, this current “best-fit” model is
523 generated based on the fact that we have the full information of the drainage experiment. While
524 this may be useful as a hybrid workflow to calculate properties that are difficult or impossible to
525 measure in unsteady-state experiments, notably relative permeability, performing the experiment
526 itself is time-consuming and complex. Therefore, further work should point out if the Pct-based
527 rock-typing can serve as a baseline to develop more straightforward sub-rock typing methods.

528 **Acknowledgments, Samples, and Data**

529 Veerle Cnudde and Arjen Mascini (Ghent University) are gratefully acknowledged for their advice
530 and support during the experiment and the analysis. Shan Wang holds a PhD scholarship funded
531 by the China Scholarship Council (CSC Grant 201906440157). Tom Bultreys is a postdoctoral
532 fellow of the Research Foundation–Flanders (FWO) and acknowledges its support under grant
533 12X0919N. The special research fund of the Ghent University (BOF-UGent) is acknowledged for
534 the financial support to the UGCT Centre of Expertise (BOF.EXP.2017.0007). Leonardo Ruspini
535 would like to thank the Norwegian Research Council for partially supporting this research (grant
536 296093). The data is made available on the Digital Rocks Portal (www.digitalrocksportal.org).

537 **References**

- 538 Alhashmi, Z., Blunt, M. J., & Bijeljic, B. (2015). Predictions of dynamic changes in reaction rates
539 as a consequence of incomplete mixing using pore scale reactive transport modeling on
540 images of porous media. *Journal of contaminant hydrology*, 179, 171-181.
541 <https://doi.org/10.1016/j.jconhyd.2015.06.004>
- 542 Alyafei, N., & Blunt, M. J. (2016). The effect of wettability on capillary trapping in carbonates.
543 *Advances in Water Resources*, 90, 36-50. <https://doi.org/10.1016/j.advwatres.2016.02.001>
- 544 Alyafei, N., Raeini, A. Q., Paluszny, A., & Blunt, M. J. (2015). A sensitivity study of the effect of
545 image resolution on predicted petrophysical properties. *Transport in Porous Media*, 110(1),
546 157-169. <https://doi.org/10.1007/s11242-015-0563-0>
- 547 Amid, A., Mignard, D., & Wilkinson, M. (2016). Seasonal storage of hydrogen in a depleted
548 natural gas reservoir. *International journal of hydrogen energy*, 41(12), 5549-5558.
549 <https://doi.org/10.1016/j.ijhydene.2016.02.036>

- 550 Arif, M., Lebedev, M., Barifcani, A., & Iglauer, S. (2017). CO₂ storage in carbonates: Wettability
551 of calcite. *International Journal of Greenhouse Gas Control*, *62*, 113-121.
552 <https://doi.org/10.1016/j.ijggc.2017.04.014>
- 553 Bauer, D., Youssef, S., Fleury, M., Bekri, S., Rosenberg, E., & Vizika, O. (2012). Improving the
554 estimations of petrophysical transport behavior of carbonate rocks using a dual pore network
555 approach combined with computed microtomography. *Transport in porous media*, *94*(2),
556 505-524. <http://dx.doi.org/10.1007/s11242-012-9941-z>
- 557 Bera, B., Mitra, S. K., & Vick, D. (2011). Understanding the micro structure of Berea Sandstone
558 by the simultaneous use of micro-computed tomography (micro-CT) and focused ion beam-
559 scanning electron microscopy (FIB-SEM). *Micron*, *42*(5), 412-418.
560 <https://doi.org/10.1016/j.micron.2010.12.002>
- 561 Blunt, M. J. (2001). Flow in porous media—pore-network models and multiphase flow. *Current*
562 *opinion in colloid & interface science*, *6*(3), 197-207. [https://doi.org/10.1016/S1359-](https://doi.org/10.1016/S1359-0294(01)00084-X)
563 [0294\(01\)00084-X](https://doi.org/10.1016/S1359-0294(01)00084-X)
- 564 Blunt, M. J., Bijeljic, B., Dong, H., Gharbi, O., Iglauer, S., Mostaghimi, P., Paluszny, A., &
565 Pentland, C. (2013). Pore-scale imaging and modelling. *Advances in Water resources*, *51*,
566 197-216. <https://doi.org/10.1016/j.advwatres.2012.03.003>
- 567 Boone, M. A., De Kock, T., Bultreys, T., De Schutter, G., Vontobel, P., Van Hoorebeke, L., &
568 Cnudde, V. (2014). 3D mapping of water in oolitic limestone at atmospheric and vacuum
569 saturation using X-ray micro-CT differential imaging. *Materials characterization*, *97*, 150-
570 160. <https://doi.org/10.1016/j.matchar.2014.09.010>
- 571 Bortone, I., Di Nardo, A., Di Natale, M., Erto, A., Musmarra, D., & Santonastaso, G. F. (2013).
572 Remediation of an aquifer polluted with dissolved tetrachloroethylene by an array of wells
573 filled with activated carbon. *Journal of hazardous materials*, *260*, 914-920.
574 <https://doi.org/10.1016/j.jhazmat.2013.06.050>
- 575 Brooks, R. H., & Corey, A. T. (1964). Hydraulic properties of porous media (Doctoral dissertation,
576 Colorado State University. Libraries).
- 577 Brooks, R. H., & Corey, A. T. (1966). Properties of porous media affecting fluid flow. *Journal of*
578 *the irrigation and drainage division*, *92*(2), 61-88. <https://doi.org/10.1061/JRCEA4.0000425>
- 579 Bultreys, T., Boone, M. A., Boone, M. N., De Schryver, T., Masschaele, B., Van Hoorebeke, L.,
580 & Cnudde, V. (2016a). Fast laboratory-based micro-computed tomography for pore-scale

- 581 research: Illustrative experiments and perspectives on the future. *Advances in water resources*,
582 95, 341-351. <https://doi.org/10.1016/j.advwatres.2015.05.012>
- 583 Bultreys, T., De Boever, W., & Cnudde, V. (2016b). Imaging and image-based fluid transport
584 modeling at the pore scale in geological materials: A practical introduction to the current
585 state-of-the-art. *Earth-Science Reviews*, 155, 93-128.
586 <https://doi.org/10.1016/j.earscirev.2016.02.001>
- 587 Bultreys, T., Lin, Q., Gao, Y., Raeni, A. Q., AlRatrou, A., Bijeljic, B., & Blunt, M. J. (2018).
588 Validation of model predictions of pore-scale fluid distributions during two-phase flow.
589 *Physical Review E*, 97(5), 053104. <https://doi.org/10.1103/PhysRevE.97.053104>
- 590 Bultreys, T., Singh, K., Raeni, A. Q., Ruspini, L. C., Øren, P. E., Berg, S., Rücker, M., Bijeljic,
591 B., & Blunt, M. J. (2020). Verifying pore network models of imbibition in rocks using time-
592 resolved synchrotron imaging. *Water Resources Research*, 56(6), e2019WR026587.
593 <https://doi.org/10.1029/2019WR026587>
- 594 Bultreys, T., Stappen, J. V., Kock, T. D., Boever, W. D., Boone, M. A., Hoorebeke, L. V., &
595 Cnudde, V. (2016c). Investigating the relative permeability behavior of microporosity-rich
596 carbonates and tight sandstones with multiscale pore network models. *Journal of Geophysical*
597 *Research: Solid Earth*, 121(11), 7929-7945. <https://doi.org/10.1002/2016JB013328>
- 598 Bultreys, T., Van Hoorebeke, L., & Cnudde, V. (2015). Multi-scale, micro-computed tomography-
599 based pore network models to simulate drainage in heterogeneous rocks. *Advances in Water*
600 *Resources*, 78, 36-49. <https://doi.org/10.1016/j.advwatres.2015.02.003>
- 601 Burchette, T. P. (2012). Carbonate rocks and petroleum reservoirs: a geological perspective from
602 the industry. *Geological Society, London, Special Publications*, 370(1), 17-37.
603 <https://doi.org/10.1144/SP370.14>
- 604 Ciobanu, C. L., Cook, N. J., Utsunomiya, S., Pring, A., & Green, L. (2011). Focussed ion beam-
605 transmission electron microscopy applications in ore mineralogy: Bridging micro-and
606 nanoscale observations. *Ore Geology Reviews*, 42(1), 6-31.
607 <https://doi.org/10.1016/j.oregeorev.2011.06.012>
- 608 Cnudde, V., & Boone, M. N. (2013). High-resolution X-ray computed tomography in geosciences:
609 A review of the current technology and applications. *Earth-Science Reviews*, 123, 1-17.
610 <https://doi.org/10.1016/j.earscirev.2013.04.003>

- 611 De Boever, W., Derluyn, H., Van Loo, D., Van Hoorebeke, L., & Cnudde, V. (2015). Data-fusion
612 of high resolution X-ray CT, SEM and EDS for 3D and pseudo-3D chemical and structural
613 characterization of sandstone. *Micron*, 74, 15-21.
614 <https://doi.org/10.1016/j.micron.2015.04.003>
- 615 Devarapalli, R. S., Islam, A., Faisal, T. F., Sassi, M., & Jouiad, M. (2017). Micro-CT and FIB–
616 SEM imaging and pore structure characterization of dolomite rock at multiple scales. *Arabian*
617 *Journal of Geosciences*, 10(16), 1-12. <https://doi.org/10.1007/s12517-017-3120-z>
- 618 Dierick, M., Van Loo, D., Masschaele, B., Van den Bulcke, J., Van Acker, J., Cnudde, V., & Van
619 Hoorebeke, L. (2014). Recent micro-CT scanner developments at UGCT. *Nuclear*
620 *Instruments and Methods in Physics Research Section B: Beam Interactions with Materials*
621 *and Atoms*, 324, 35-40. <https://doi.org/10.1016/j.nimb.2013.10.051>
- 622 Dong, H., & Blunt, M. J. (2009). Pore-network extraction from micro-computerized-tomography
623 images. *Physical review E*, 80(3), 036307. <https://doi.org/10.1103/PhysRevE.80.036307>
- 624 Gao, Y., Lin, Q., Bijeljic, B., & Blunt, M. J. (2017). X-ray microtomography of intermittency in
625 multiphase flow at steady state using a differential imaging method. *Water Resources*
626 *Research*, 53(12), 10274-10292. <https://doi.org/10.1002/2017WR021736>
- 627 Gharbi, O., & Blunt, M. J. (2012). The impact of wettability and connectivity on relative
628 permeability in carbonates: A pore network modeling analysis. *Water Resources Research*,
629 48(12). <https://doi.org/10.1029/2012WR011877>
- 630 Ghous, A., Senden, T. J., Sok, R. M., Sheppard, A. P., Pinczewski, V. W., & Knackstedt, M. A.
631 (2007, January). 3D characterisation of microporosity in carbonate cores. In *SPWLA Middle*
632 *East Regional Symposium*. Society of Petrophysicists and Well-Log Analysts.
- 633 Han, M., Fleury, M., & Levitz, P. (2007, September). Effect of the pore structure on resistivity
634 index curves. In *International Symposium of the Society of Core Analysts* (Vol. 34). Canada:
635 Society of Core Analysts.
- 636 Jiang, Z., Van Dijke, M. I. J., Sorbie, K. S., & Couples, G. D. (2013). Representation of multiscale
637 heterogeneity via multiscale pore networks. *Water resources research*, 49(9), 5437-5449.
638 <https://doi.org/10.1002/wrcr.20304>
- 639 Joekar-Niasar, V., & Hassanizadeh, S. M. (2012). Analysis of fundamentals of two-phase flow in
640 porous media using dynamic pore-network models: A review. *Critical reviews in*

- 641 *environmental science and technology*, 42(18), 1895-1976.
642 <https://doi.org/10.1080/10643389.2011.574101>
- 643 Lai, J., Wang, G., Wang, Z., Chen, J., Pang, X., Wang, S., Zhou, Z., He, Z., Qin, Z., & Fan, X.
644 (2018). A review on pore structure characterization in tight sandstones. *Earth-Science*
645 *Reviews*, 177, 436-457. <https://doi.org/10.1016/j.earscirev.2017.12.003>
- 646 Lin, Q., Al-Khulaifi, Y., Blunt, M. J., & Bijeljic, B. (2016). Quantification of sub-resolution
647 porosity in carbonate rocks by applying high-salinity contrast brine using X-ray
648 microtomography differential imaging. *Advances in water resources*, 96, 306-322.
649 <https://doi.org/10.1016/j.advwatres.2016.08.002>
- 650 Lin, Q., Bijeljic, B., Rieke, H., & Blunt, M. J. (2017). Visualization and quantification of capillary
651 drainage in the pore space of laminated sandstone by a porous plate method using differential
652 imaging X-ray microtomography. *Water Resources Research*, 53(8), 7457-7468.
653 <https://doi.org/10.1002/2017WR021083>
- 654 Lin, W., Li, X., Yang, Z., Manga, M., Fu, X., Xiong, S., Gong, A., Chen, G., Li, H., Pei, L., Li, S.,
655 Zhao, X., & Wang, X. (2019). Multiscale digital porous rock reconstruction using template
656 matching. *Water Resources Research*, 55(8), 6911-6922.
657 <https://doi.org/10.1029/2019WR025219>
- 658 Mason, G., & Morrow, N. R. (1991). Capillary behavior of a perfectly wetting liquid in irregular
659 triangular tubes. *Journal of Colloid and Interface Science*, 141(1), 262-274.
660 [https://doi.org/10.1016/0021-9797\(91\)90321-X](https://doi.org/10.1016/0021-9797(91)90321-X)
- 661 Mehmani, A., & Prodanović, M. (2014). The effect of microporosity on transport properties in
662 porous media. *Advances in Water Resources*, 63, 104-119.
663 <https://doi.org/10.1016/j.advwatres.2013.10.009>
- 664 Mehmani, A., Verma, R., & Prodanović, M. (2020). Pore-scale modeling of carbonates. *Marine*
665 *and Petroleum Geology*, 114, 104141. <https://doi.org/10.1016/j.marpetgeo.2019.104141>
- 666 Menke, H., Gao, Y., Linden, S., & Andrew, M. (2019). Using nano-XRM and high-contrast
667 imaging to inform micro-porosity permeability during Stokes-Brinkman single and two-
668 phase flow simulations on micro-CT images. <https://doi.org/10.31223/osf.io/ubg6p>
- 669 Mouli-Castillo, J., Wilkinson, M., Mignard, D., McDermott, C., Haszeldine, R. S., & Shipton, Z.
670 K. (2019). Inter-seasonal compressed-air energy storage using saline aquifers. *Nature Energy*,
671 4(2), 131-139. <https://doi.org/10.1038/s41560-018-0311-0>

- 672 Mousavi, M., Prodanovic, M., & Jacobi, D. (2013). New classification of carbonate rocks for
673 process-based pore-scale modeling. *SPE Journal*, 18(02), 243-263.
674 <https://doi.org/10.2118/163073-PA>
- 675 Nono, F., Bertin, H., & Hamon, G. (2014, January). An experimental investigation of the oil
676 recovery in the transition zone of carbonate reservoirs taking into account wettability change.
677 In *IPTC 2014: International Petroleum Technology Conference* (pp. cp-395). European
678 Association of Geoscientists & Engineers. [https://doi.org/10.3997/2214-4609-pdb.395.IPTC-](https://doi.org/10.3997/2214-4609-pdb.395.IPTC-17640-MS)
679 [17640-MS](https://doi.org/10.3997/2214-4609-pdb.395.IPTC-17640-MS)
- 680 Olayiwola, S. O., & Dejam, M. (2019). A comprehensive review on interaction of nanoparticles
681 with low salinity water and surfactant for enhanced oil recovery in sandstone and carbonate
682 reservoirs. *Fuel*, 241, 1045-1057. <https://doi.org/10.1016/j.fuel.2018.12.122>
- 683 Øren, P. E., Ruspini, L. C., Saadatfar, M., Sok, R. M., Knackstedt, M., & Herring, A. (2019). In-
684 situ pore-scale imaging and image-based modelling of capillary trapping for geological
685 storage of CO₂. *International Journal of Greenhouse Gas Control*, 87, 34-43.
686 <https://doi.org/10.1016/j.ijggc.2019.04.017>
- 687 Pak, T., Butler, I. B., Geiger, S., van Dijke, M. I., & Sorbie, K. S. (2015). Droplet fragmentation:
688 3D imaging of a previously unidentified pore-scale process during multiphase flow in porous
689 media. *Proceedings of the National Academy of Sciences*, 112(7), 1947-1952.
690 <https://doi.org/10.1073/pnas.1420202112>
- 691 Pan, C., Hilpert, M., & Miller, C. T. (2004). Lattice-Boltzmann simulation of two-phase flow in
692 porous media. *Water Resources Research*, 40(1). <https://doi.org/10.1029/2003WR002120>
- 693 Prodanović, M., Mehmani, A., & Sheppard, A. P. (2015). Imaged-based multiscale network
694 modelling of microporosity in carbonates. *Geological Society, London, Special Publications*,
695 406(1), 95-113. <https://doi.org/10.1144/SP406.9>
- 696 Raeini, A. Q., Blunt, M. J., & Bijeljic, B. (2012). Modelling two-phase flow in porous media at
697 the pore scale using the volume-of-fluid method. *Journal of Computational Physics*, 231(17),
698 5653-5668. <https://doi.org/10.1016/j.jcp.2012.04.011>
- 699 Ruspini, L. C., Farokhpoor, R., & Øren, P. E. (2017). Pore-scale modeling of capillary trapping in
700 water-wet porous media: A new cooperative pore-body filling model. *Advances in Water*
701 *Resources*, 108, 1-14. <https://doi.org/10.1016/j.advwatres.2017.07.008>

- 702 Ruspini, L. C., Lindkvist, G., Bakke, S., Alberts, L., Carnerup, A. M., & Øren, P. E. (2016, May).
703 A Multi-Scale Imaging and Modeling Workflow for Tight Rocks. In *SPE Low Perm*
704 *Symposium*. Society of Petroleum Engineers.
- 705 Ruspini, L. C., Øren, P. E., Berg, S., Masalmeh, S., Bultreys, T., Taberner, C., Sorop, T., Marcelis,
706 F., Appel, M., Freeman, J., & Wilson, O. B. (2021). "Multiscale digital rock analysis for
707 complex rocks". Submitted to *Transport in Porous Media*.
- 708 Shanley, K. W., Cluff, R. M., & Robinson, J. W. (2004). Factors controlling prolific gas production
709 from low-permeability sandstone reservoirs: Implications for resource assessment, prospect
710 development, and risk analysis. *AAPG bulletin*, 88(8), 1083-1121.
711 <https://doi.org/10.1306/03250403051>
- 712 Wang, J., Song, H., & Wang, Y. (2020). Investigation on the micro-flow mechanism of enhanced
713 oil recovery by low-salinity water flooding in carbonate reservoir. *Fuel*, 266, 117156.
714 <https://doi.org/10.1016/j.fuel.2020.117156>
- 715 Wirth, R. (2009). Focused Ion Beam (FIB) combined with SEM and TEM: Advanced analytical
716 tools for studies of chemical composition, microstructure and crystal structure in geomaterials
717 on a nanometre scale. *Chemical Geology*, 261(3-4), 217-229.
718 <https://doi.org/10.1016/j.chemgeo.2008.05.019>
- 719 Xiong, Q., Baychev, T. G., & Jivkov, A. P. (2016). Review of pore network modelling of porous
720 media: Experimental characterisations, network constructions and applications to reactive
721 transport. *Journal of contaminant hydrology*, 192, 101-117.
722 <https://doi.org/10.1016/j.jconhyd.2016.07.002>
- 723 Youssef, S., Han, M., Bauer, D., Rosenberg, E., Bekri, S., Fleury, M., & Vizika, O. (2008, October).
724 High resolution μ -CT combined to numerical models to assess electrical properties of bimodal
725 carbonates. In *International Symposium of Core Analysts* (pp. 1-12).